Deformation mechanisms in PBT at elevated temperatures

Laurent Farge, Francois Tournilhac, Sandrine Hoppe, Javier Perez, Isabelle Bihannic, Jérémy Bianchin, Quentin-Arthur Poutrel, Julien Boisse, Stéphane André

▶ **To cite this version:**

Laurent Farge, Francois Tournilhac, Sandrine Hoppe, Javier Perez, Isabelle Bihannic, et al.. Deformation mechanisms in PBT at elevated temperatures. Materials Today Communications, 2023, 36, pp.106774. 10.1016/j.mtcomm.2023.106774 . hal-03982510v2

HAL Id: hal-03982510
https://hal.univ-lorraine.fr/hal-03982510v2

Submitted on 11 Oct 2023

HAL is a multi-disciplinary open access archive for the deposit and dissemination of scientific research documents, whether they are published or not. The documents may come from teaching and research institutions in France or abroad, or from public or private research centers.

L'archive ouverte pluridisciplinaire **HAL**, est destinée au dépôt et à la diffusion de documents scientifiques de niveau recherche, publiés ou non, émanant des établissements d'enseignement et de recherche français ou étrangers, des laboratoires publics ou privés.

Deformation mechanisms in PBT at elevated temperatures

Laurent FARGE[1], François TOURNILHAC[2], Sandrine HOPPE[3], Javier PEREZ[4], Isabelle BIHANNIC[5,6], Jérémy BIANCHIN[1], Quentin-Arthur POUTREL[1], Julien BOISSE[1], Stéphane ANDRÉ[1,6]

https://doi-org.bases-doc.univ-lorraine.fr/10.1016/j.mtcomm.2023.106774

1 Université de Lorraine, CNRS, LEMTA, F-54000 Nancy, France

2 Molecular, Macromolecular Chemistry, and Materials, ESPCI Paris, PSL Research University, 10 Rue Vauquelin, F-75005 Paris, France

3 Université de Lorraine, CNRS, LRGP, F-54000 Nancy, France

4 Synchrotron SOLEIL, L'Orme des Merisiers, Saint-Aubin, BP 48, 91192 Gif-sur-Yvette Cedex, France

5 Université de Lorraine, CNRS, LIEC, F-54000 Nancy, France

6 Cogitamus Laboratory, Paris, France

Abstract

Plastic deformation mechanisms of Polybutylene terephthalate (PBT) are investigated at 120°C, 150°C and 180°C using tensile experiments, 2D digital image correlation, wide and small angle X-ray scattering measurements.

Plots of nominal stress vs true strain (ε), true stress vs ε and Haward-Thackray representation reveal the same *I*, *II*, *III* regimes in strain ranges virtually independent of temperature. Between $\varepsilon = 0$ and the yield strain $\varepsilon_Y \approx 0.3$ (*I*) the layer morphology is preserved, the interlamellar distance increases in the drawing direction and the strain is localized in amorphous regions. Between $\varepsilon \approx 0.3$ and $\varepsilon \approx 1.0$ (*II*), amorphous chains remain describable as gaussian coils while transition from spherulitic to fibrillar morphologies occurs. Beyond $\varepsilon \approx 1.0$ (*III*) the chains are taut, the fibrillar morphology is established, additional stress

causes the transitions between polymorphs, respectively from isotropic amorphous to smectic and from α to β crystalline phases.

Keywords

PBT; Mechanical Properties; SAXS-WAXS; Structure Evolution

1 Introduction

Polybutylene terephthalate (PBT) is an engineering semi-crystalline polymer, remarkable by its relatively high melting point ($T_m \approx 225°C$), low melt viscosity, fast crystallization and low water uptake, which makes it particularly suitable for implementation by injection molding and use in electric insulation, cooking tools, electric appliances, composites etc. One of the key properties in all these applications is the mechanical resistance at high temperature. Significant efforts have been made in recent years to improve the mechanical resistance of PBT both above and below the melting point by chemical modification along the concept of vitrimers [1–6]. To understand where this improvement in performance comes from, it is necessary to analyze the deformation mechanisms of PBT at elevated temperatures (>100°C) where its heat-resistant behavior justifies its use.

The deformation mechanisms of semi-crystalline polymers are primarily studied using *in situ* SAXS/WAXS (Small/Wide Angle X-ray Scattering) measurements performed during tensile tests. To prevent specimen rupture and reach the strain level corresponding to neck stabilization, it is necessary to conduct these experiments above the glass transition temperature (T_g). Semi-crystalline polymers such as polyethylene (T_g=-110°C) [7–15] or polypropylene (T_g=-10°C) [16–20] have been extensively studied. As for PBT, its glass transition temperature higher than the ambiant ($T_g \approx 55°C$) makes the experiments more challenging and actually, we have found only one paper by Zhang et al. [21] specifically dedicated to such study. Ther authors of this article highlighted three different stages during the deformation process, each associated with specific structural changes. Nonetheless, they did not report local true strain measurements but only engineering strain values taken from the tensile machine crosshead relative displacement. Due to the complex distribution of strains along the specimen caused by necking, threshold values measured on engineering strain do not correspond to intrinsic quantities representing material's properties. Such data can then hardly be used for further studies, in particular the

understanding of PBT-based vitrimer properties, especially considering that vitrimerization alters the way strain localization (necking) occurs [5,6].

Furthermore, the highest temperature for which SAXS/WAXS measurements were reported in the Zhang et al.[21] study (120°C) is significantly smaller than the PBT melting temperature ($T_m \approx 225$°C). This study therefore does not encompass the wide temperature range where PBT is already used in practice (T<140°C), as well as the temperature range (T>140°C) where its utilization could be extended through reinforcement strategies such as vitrimerization.

With exception of the aforementioned paper [21], no set of SAXS/WAXS data were found for isotropic PBT deformed above T_g. However, it should be noted that interesting results have been obtained at room temperature using WAXS in the case of oriented PBT subjected to a tensile force [22–27]. It was found that a reversible phase transition between the α and β triclinic forms occurs at strains between 4% and 12%. This transition proceeds from a change in the glycol residue conformation from the *gauche-trans-gauche* sequence (α form) to a nearly all-*trans* sequence (β form) where the polymer chains are near full extension (Table 1). As a result, the *c* parameter (chain axis) of the triclinic unit cell significantly changes during the α → β transition (from *c* = 11.67 Å in the α-form to *c* = 12.90 Å in the β form) in a discontinuous manner where no intermediate state was reported [23]. On the other hand, the variations of the five other parameters of the triclinic cell are very small during the transition.

Smectic structures have also been observed in amorphous PBT [28,29]—obtained from molten state by quick quenching —and in other amorphous polyesters subjected to stretching below T_g, PET (polyethylene terephthalate) [30,31]and PEN (polyethylene naphtalate) [32].

In this study, synchrotron *in situ* X-ray scattering experiments were carried out to analyze the deformation mechanisms of a non-oriented PBT subjected to tensile drawing to large strains. A special heating device was designed to carry out measurements at elevated temperatures close to T_m (up to 180°C). Prior to X-ray measurements, calibration experiments were performed at each temperature, in order to access the true strain value for any position of the crosshead. The processing of the mechanical

data is therefore significantly different from that of Zhang et al.[21], insofar the quantity hereby noted ε is the true strain, measured at the center of the specimen, precisely where the X-ray beam passes through. This made it possible to define the boundaries of the different deformation regimes at each temperature in ε-values, intrinsic to the constitutive law of the material. Furthermore, the orientational effect on the α–β transition was studied, and the appearance of a smectic structure at large strains was observed in conditions not previously reported.

2 Materials and Methods

2.1 PBT production and specimen shape

The PBT studied in this work was provided by DuPont in pellet form (Material reference: CRASTIN FGS600F40). The specimens were produced in a DSM Xplore µcompounder at 270°C. The rotational speed of the two µcompounder screws was 100 rpm. At the µcompounder outlet, the melt was transferred to a shooting pot and injected into a mold in shape of a tensile specimen (see Figure S1 in the supporting information). A 4 mm length flat part was machined on the specimen lateral faces to promote a uniaxial stress state in the center of the specimen (see Figure S2 for specimen dimensions). Using this geometry, the necking develops in the specimen central region, exactly where the X-ray scattering measurement is carried out. During a previous study [5], DSC (Differential Scanning Calorimetry) measurements were performed on the same PBT and the measured glass temperature, melt temperature and crystallinity were found to be 50°C, 225°C and 34% in mass fraction respectively.

2.2 *In situ* X-ray scattering measurements during tensile testing

2.2.1 Experimental set-up

The experiments were carried out using a Kammrath & Weiss mini-machine specifically designed for *in situ* X-ray scattering studies with synchrotron radiation. The two mini-machine crossheads move apart from each other at constant speed $\dot{u}$ = 20 µms^{-1} so that the displacement of the central specimen point

— where the X-ray beam passes through the specimen — is zero. To perform high-temperature tensile tests, it was not possible to put the entire tensile machine in a heat chamber because the machine electrical and electronic components (controlling device, sensors) are not intended to work at temperatures required for our experiments (up to 180°C). We were therefore forced to design a specific heating device for this study. It consists of a heating resistance included in a small metal part that surrounds the specimen central region (see Figure 1a). As a result, only the specimen central part is subjected to high temperatures, which ensures the proper functioning of the tensile machine and of its electronics. Two apertures were cut in the heating device in front and rear faces to let the X-ray beam pass through the specimen. The tensile mini-machine was oriented horizontally to avoid gravity natural convection, which might make necking to initiate above the specimen center.

The tensile tests were interrupted when the displacement between the two crossheads was 15 mm. The deformation state in the specimen center was characterized by the value of the true longitudinal strain: $\varepsilon = \ln \lambda$. λ is the draw ratio defined by $\lambda = \ell/\ell_0$ where ℓ_0 is a small length element taken in the specimen center along the tensile axis in the initial state. ℓ is the current size of this length element during the tensile test. The nominal stress is given by $\sigma_N = F/S_0$, where S_0 is the 4×4 mm^2 area of the central cross-section.

Assuming an isochoric deformation process (see paragraph SI1 in the supporting information), the true stress that accounts for the decreasing cross-sectional area is given by: $\sigma_V = \sigma_N e^{\varepsilon}$.

Prior to synchrotron experiments and at all targeted temperatures, 2D Digital Image Correlation (2D DIC) experiments were carried out through the heating device aperture in order to measure the strain evolution $\varepsilon(t)$ during the tensile tests (Figure 2a).

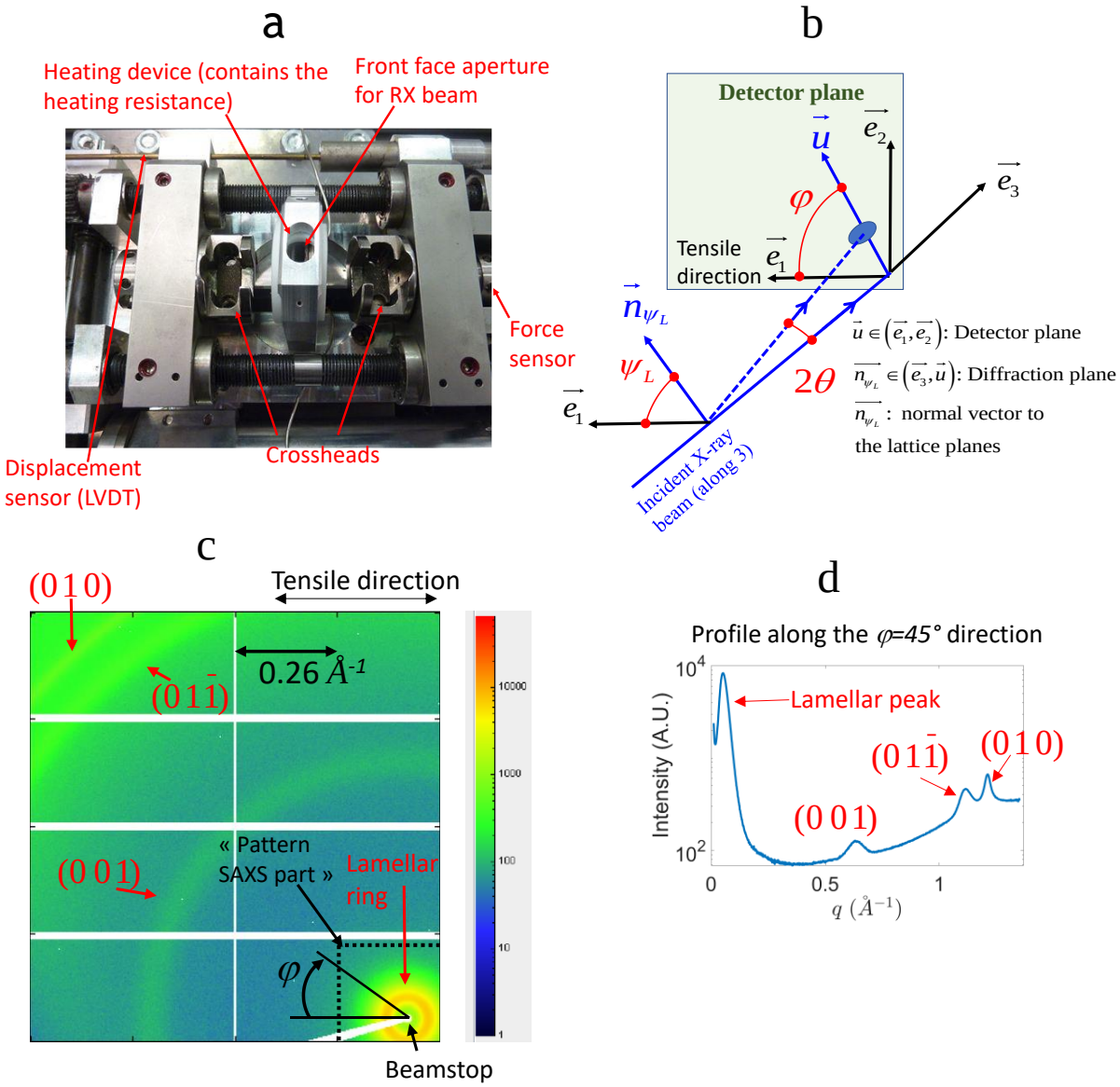

Figure 1 Experimental set-up. a) Tensile mini-machine equipped with a heating device specifically dedicated to synchrotron studies. b) Scheme of the X-ray scattering experiment geometry, c) Example of X-ray pattern measured at the initial state ($\varepsilon = 0$) at 120°C and d) Intensity profile along the $\varphi = 45°$ direction.

The principle of the 2D DIC measurement is illustrated in Figure S3. The $\varepsilon(t)$ curves are found to depend little on temperature even though the final quasi-constant strain is slightly higher at 180°C. These results were confirmed in an independent way through the analysis of the transmission signal that was measured

during the X-Ray scattering experiments. During the test, the transmission increases due to thickness reduction. Using the Beer-Lambert law and the assumption of transversally isotropic and isochoric deformation process, a second evaluation of $\varepsilon(t)$ was achieved, from the evolution of the transmission signal. A satisfactory agreement was found between the two procedures (see Figure S4), which supports that the approximation of isochore deformation is valid. In this study only the $\varepsilon(t)$ values obtained by DIC measurements will be used.

2.2.2 X-ray scattering measurement

The X-ray scattering measurements were performed on the SWING beamline at the SOLEIL synchrotron.

The radiation wavelength was 0.77489 Å (16 keV). Measurements were made at a sample-detector distances of 1244 mm for three test temperatures: 120°C, 150°C and 180°C. 75 patterns were *in situ* recorded every 10 seconds during a single tensile test with a 1 s acquisition time. The scheme of the experiment geometry is shown in Figure 1b. An example of pattern measured at 120°C and corresponding to the initial undeformed state is shown in Figure 1c. The lamellar ring is visible in the right-down part of the image corresponding to the "SAXS part" of the pattern. The detector position was chosen so that a full quadrant — azimuthal angles (φ) ranging from 0° to 90° —is covered for the (001) reflection. A part of the $(01\bar{1})$ and (010) reflections can also be seen in upper-left part of the pattern ($\varphi \approx 45°$), as it can be checked on an intensity profile measured along the $\varphi = 45°$ direction (Figure 1d).

In this study, we will mainly analyze the (001) reflection, and the evolution of the correlation distance corresponding to the lamella periodic organization. In both cases, the Bragg angle θ is very small: $\theta < 0.25°$ for the lamellar periodic morphology (correlation distance of about 100 Å), and $\theta \approx 2°$ for the (001) reflection (spacing between crystallographic planes≃10 Å). The Polony relation: $\cos\psi_L = \cos\theta\cos\varphi$— linking the Bragg angle θ, the angle ψ_L between the tensile direction and the

normal to the lattices ($\vec{n}_{\psi_L}$) and the azimuthal angle φ defined on the scattering pattern (Figure 1c) — leads to consider that $\psi_L \approx \varphi$.

In the SAXS part of the pattern, the evolution of the correlation distance associated with lamella scattering was measured along the drawing direction both with (d^{Ltz}) and without (d) the Lorentz correction. The details of the determination of d^{Ltz} and d are given in the supplementary information (paragraph SI2).

Based on a two-phase model of the lamellar morphology and using the procedure described by Strobl et al. [33] (illustrated in Figure S5 and detailed in SI3 of the supplementary data), the proportion of crystalline phase was extracted from the SAXS patterns measured at the initial state by analyzing the characteristics of the correlation function $K(r)$ that is defined as follows:

$$K(r) = \frac{\int_0^\infty I(q) q^2 \cos(qr) dq}{\int_0^\infty I(q) q^2 dq} \qquad \text{Equation 1}$$

The SAXS pattern is assumed to be isotropic but the method is sometimes extended to oriented morphologies [34].

In order to identify the different possible crystalline phases for PBT (α or β forms), complementary measurements were performed at 150°C using a sample-detector distance of 726 mm (see Figure S6a for the pattern recorded before deformation). In addition to the (001), $(01\bar{1})$ and (010) reflections, parts of the $(1\,1\,1)$, $(1\bar{1}\,0)$, (100) and $(1\bar{1}\,1)$ reflections were also identified on the patterns. Unfortunately, it was not possible to obtain the reflection intensities on a complete quadrant. At the heating device outlet, the aperture dimension along the tensile direction is too small to allow the photons to go out if the scattering angle is too large. Incidentally, this blind sector is also the region where uniaxially oriented crystals are not expected to produce diffraction signals, because nodes located along the drawing direction, especially at large q do not intercept the Ewald sphere anymore when orientation is strong.

3 Results and discussion

3.1 Tensile testing

In Figure 2b, we show the evolution of the nominal stress (σ_N) versus the true strain (ε) for tensile tests performed at 120°C, 150°C and 180°C. These three curves exhibit three different stages which start and end at well-defined values of the true strain, approximately independent of temperature. These three stages can be described as follows. From $\varepsilon = 0$ to $\varepsilon \approx 0.3$ (strain range *I*), the stress strongly increases until the yield point. The yield strain (ε_Y) is approximately the same for the three test temperatures ($\varepsilon_Y \approx 0.29$ at 120°C, $\varepsilon_Y \approx 0.32$ at 150°C, $\varepsilon_Y \approx 0.35$ at 180°C). From $\varepsilon \approx 0.3$ to $\varepsilon \approx 1.0$ (strain range *II*), the nominal stress only shows small variations. Strain range *III* begins approximately at $\varepsilon \approx 1.0$ for the three test temperatures and corresponds to an abrupt increase of σ_N. It is also interesting to analyze these tensile tests using the true stress σ_V that correctly accounts for the decreasing cross-sectional area. Different representations are possible. In Figure S7, we show the true stress-true strain curves $\sigma_V(\varepsilon)$.

In Figure 2c, the true stress σ_V is plotted as a function of $HT = \lambda^2 - 1/\lambda = e^{2\varepsilon} - e^{-\varepsilon}$, which is the representation associated with the Haward-Thackray model [35,36] (see also SI4). In both cases, the transitions between regimes *I*, *II* and *III* are detected for the same values of true strain.

In strain range *II*, the nominal stress is nearly constant while an approximately linear regime corresponding to a network shear modulus of a few MPa is observed in the Haward-Thackray representation (Figure 2c) (linearity in strain range II would certainly be even better if test were performed at constant strain rate). According to the Haward-Thackray model, this means that the Gaussian chain approximation is valid in describing the macromolecular network stretching accompanying the plastic flow. On the other hand, an abrupt stress increase that is observed during strain range *III* occurs when the macromolecular network is fully extended (Figure 2b,c and Figure S7). The chains are taut and the Gaussian chain approximation is no longer valid. Unwinding part of the chains from the crystals is then necessary to allow further deformation.

Interestingly, the three evidenced regimes, separated by the same strain thresholds ($\varepsilon \approx 0.30$ and $\varepsilon \approx 1.0$), also appear on the $\varepsilon(t)$ curves in Figure 2a or S4. During strain range *II*, after the yield point, the strain rate strongly increases. During strain range *III*, the strain increase becomes very small in the neck center (≈ specimen center) because strain hardening is very strong in this zone (see Figure S7). The plastic instability migrates in other specimen regions (i.e., the two symmetrical neck shoulders) [37,38].

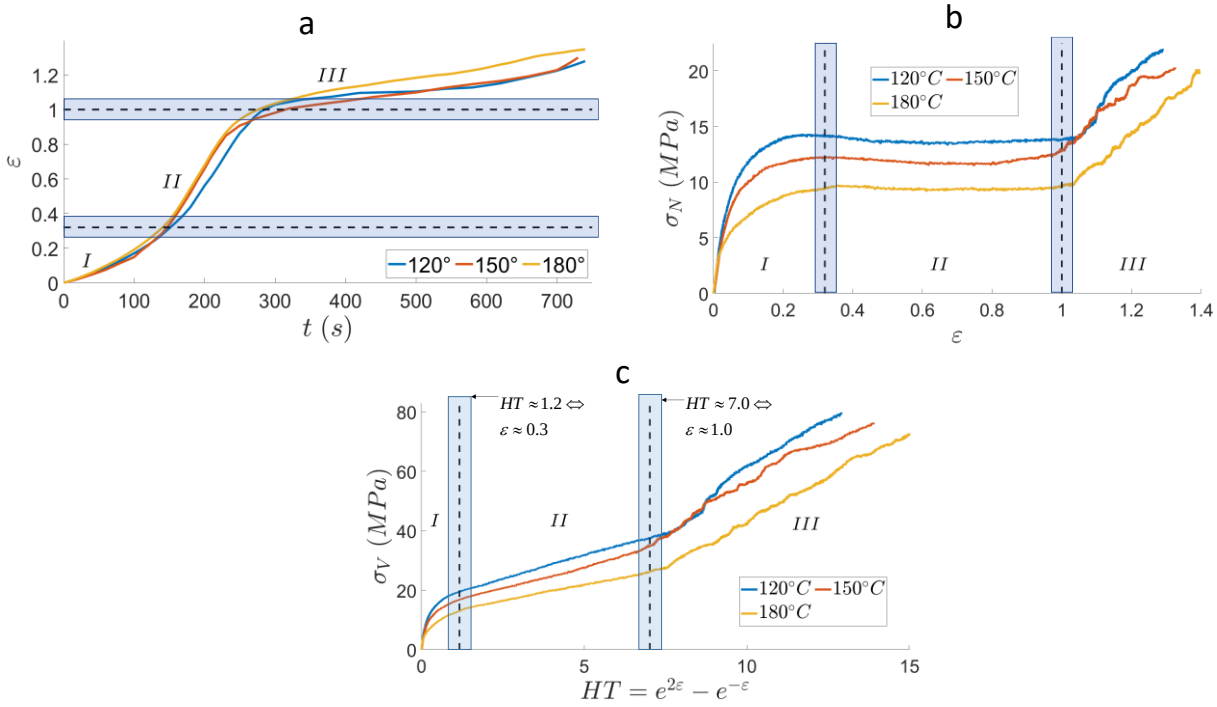

Figure 2 Mechanical testing. a) Evolution of the true longitudinal strain $\varepsilon(t)$ *measured in the specimen central cross-section, b) Evolution of the nominal stress:* $\sigma_N(\varepsilon)$ *curves, c) True stress* σ_V *versus* $e^{2\varepsilon} - e^{-\varepsilon}$ *(Haward-Thackray representation)*

3.2 SAXS analysis

3.2.1 Description of SAXS Patterns

Examples of SAXS patterns (extracted from the down-right part of the full detector plane as shown in Figure 1b) are given in Figure 3 at various strain levels and for the three test temperatures.

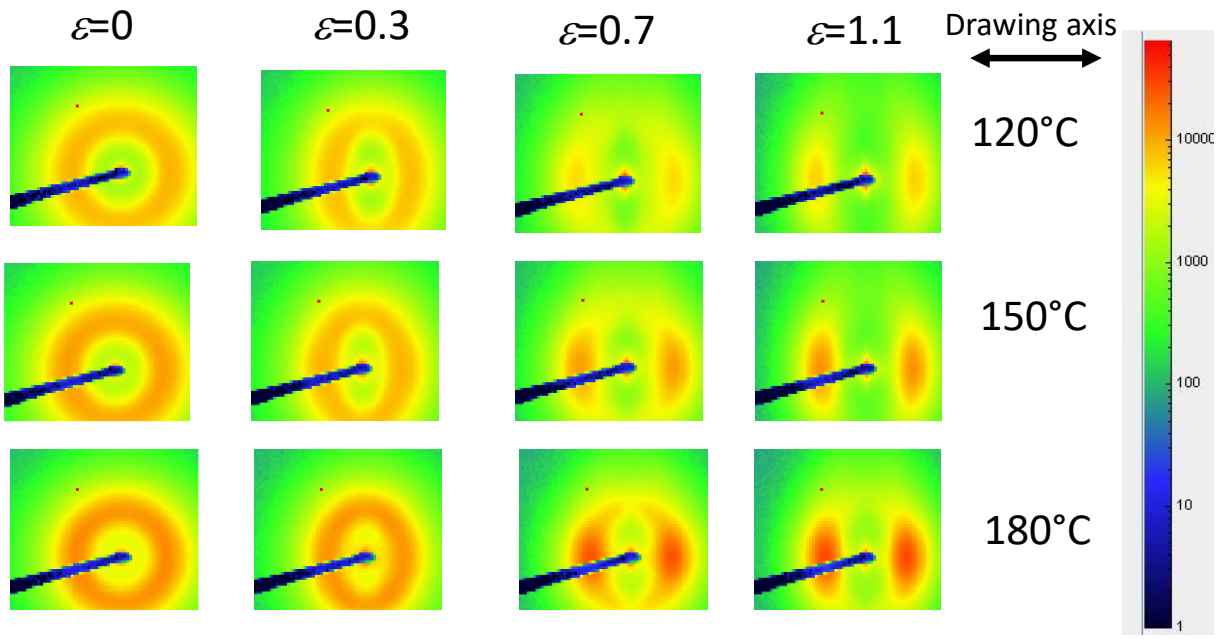

Figure 3 Examples of SAXS patterns

As expected, we can observe the circular ring associated with the isotropic lamellar morphology at the initial state ($\varepsilon = 0$). The proportion of crystalline phase extracted from the correlation function are 30.7% at 120°C, 31.2% at 150°C and 32.2% at 180°C. These values are in good agreement with the crystallinity measured by DSC (34%, see section 2.1). At the yield point ($\varepsilon \approx 0.3$), the ring is deformed because the correlation distance increases for the lamellae perpendicularly oriented with respect to the drawing axis while it decreases for the lamellae oriented along this direction. However, the intensity along the ring remains approximately constant. At larger strains ($\varepsilon = 0.7$) the lamellar ring is hardly discernible and the main feature of the SAXS patterns becomes the two intensity maxima along the horizontal axis (drawing axis) that are characteristics of the fibrillar morphology. Finally, at $\varepsilon = 1.1$, the fibrillar morphology is definitely established.

3.2.2 Analysis of the SAXS correlation distance evolution

The $d^{Lz}(\varepsilon)$ (correlation distance measured along the drawing direction with Lorentz correction) curves are plotted in Figure 4a. In the following, we analyze the evolution of the correlation distance (measured at nano-scale) in the frame of the three regimes that were identified through the variations of the macroscopic stress (Figures 2b, 2c and S7).

Evolution of the correlation distance during Stage I

As it has often been observed for semi-crystalline polymers, d^{Ltz} begins to increase [21,39–43]. The lamellae's integrity is first overall preserved and the lamellae normally oriented with respect to the tensile direction move away from each over, which causes the observed d^{Ltz} increase. Precisely at the transition between strain ranges *I* and *II* ($\varepsilon \approx 0.3$), d^{Ltz} reaches a maximum.

Stage I/Stage II Transition and evolution of the correlation distance during stage II

Next, d^{Ltz} significantly decreases from the beginning of strain range *II* at 120°C and 150°C. The lamellae's fragmentation is in progress, which leads to an increase of the number of crystalline regions per volume unit, and logically to the decrease of the correlation distance (d^{Ltz}). On the other hand, the evolution of d^{Ltz} during strain range *II* differs drastically at 180°C: instead of decreasing, the correlation distance remains nearly constant. Jiang et al. have obtained very comparable curves for the dependence of the $d^{Ltz}(\varepsilon)$ curves on temperature in the case of a high-density polyethylene [40]. They showed that during solidification from the melt, certain crystal blocks are likely to crystallize at temperatures lower than that of the tensile test carried out afterwards. During this tensile test, these crystal blocks become unstable because they are subjected to stress and melt before rapidly recrystallizing at the test temperature with higher thicknesses. This leads to an increase in d^{Ltz}, which may compensate the decrease trend due to fragmentation. This is what occurs for the test performed on PBT at 180°C (Figure 4a). On the other hand, the number of crystal block formed below 150°C during solidification is too small for the decreasing trend of d^{Ltz} caused by fragmentation to be compensated in the case of the test carried out at this temperature.

As proposed by some authors [21,44], the evolution of both the crystal $d_c(\varepsilon)$ and amorphous $d_a(\varepsilon)$ thicknesses as function of the applied strain were calculated from the correlation function $K(r)$ (Equation 1, Figure S5 and paragraph SI3). $d_c(\varepsilon)$ and $d_a(\varepsilon)$ are plotted in Figure 4b. The reliability of such a calculus can be discussed because the Lorentz correction assumes an isotropic material, which is not true during the tensile process. However, it will be shown in section 3.4 that the bias due to

anisotropy development is nearly the same at all three temperatures and consequently the $d_c(\varepsilon)$ curves difference in behavior is relevant for analyzing the temperature effect on the deformation process. Notably, referring to Figure 4b we can observe that $d_c(\varepsilon)$ increases during strain range *II* at the three test temperatures, with a more pronounced increase as the temperature rises. This confirms that the results from figure 4a during the stage *II* measurement are due to the melting of crystal blocks upon stress followed by rapid recrystallization with higher thicknesses at the test temperature.

Stage II/Stage III transition and evolution of the correlation distance during strain range III

The transition at $\varepsilon \approx 1.0$ seems to correspond to a slight increase of the $d^{Ltz}(\varepsilon)$ curves (Figure 4a). Nevertheless, this is not easy to assure because $d^{Ltz}(\varepsilon)$ seems increasing from about $\varepsilon \approx 0.8$. At these strains the polymers are strongly oriented (Figure 3) and the use of the Lorentz correction is highly questionable. Therefore, we have represented in Figure 4c the variations of the correlation distance in the "large strains" domain ($\varepsilon > 0.7$) calculated without Lorentz correction (d). The strain threshold previously highlighted at $\varepsilon \approx 1$ is well confirmed here. The $d(\varepsilon)$ evolution on the whole strain range is shown in Figure S8.

In summary, we have described the evolution of the microstructure associated with the three stages of the deformation process that were identified on the stress-strain curves (Figures 2b, c and S7): Strain range *I*: the lamellar structure is roughly preserved, strain range *II*: the morphology changes from lamellar to fibrillar, and strain range *III*: the fibrillar morphology is overall established. A schematic representation of the microstructure evolution is shown in Figure S9.

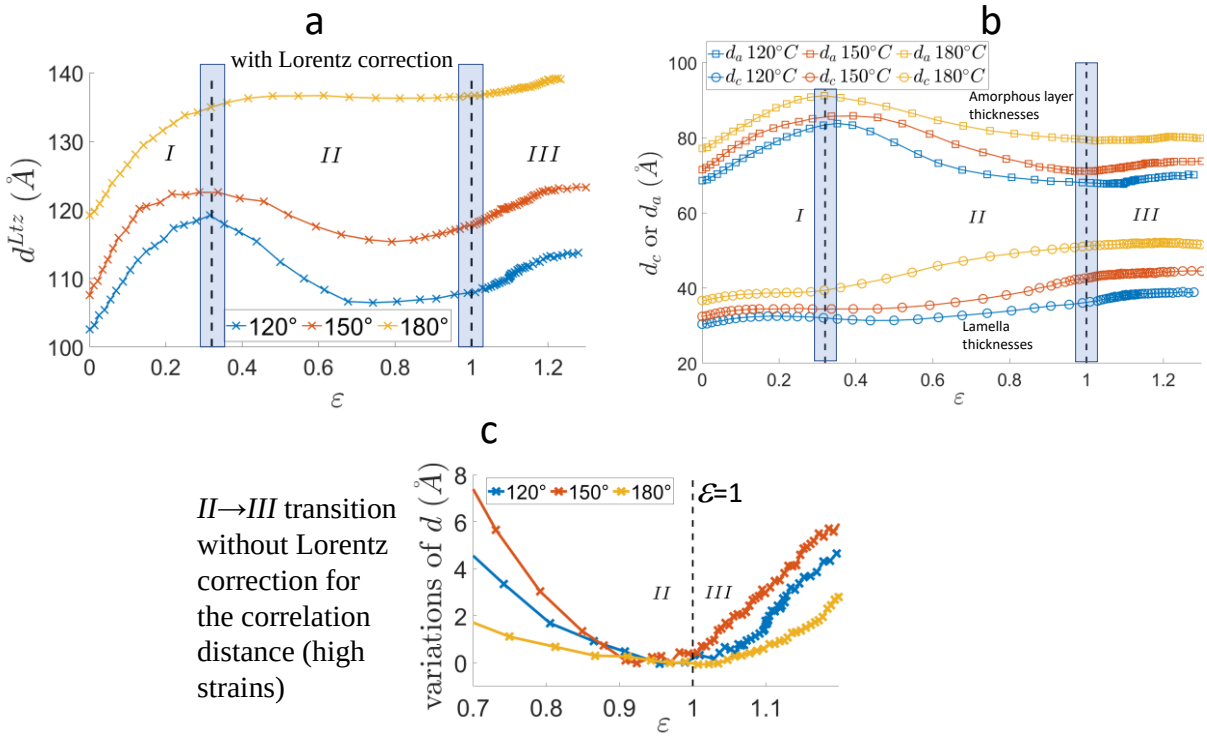

Figure 4 Characteristics lengths extracted from the SAXS patterns. a) Correlation distance calculated by using the Lorentz correction (d^{Ltz}). b) *Lamella and amorphous layer thicknesses along the drawing axis calculated using the correlation function (Equation 1). c) variations of the correlation distance around the II→III transition calculated without the Lorentz correction* (d). *Note that in Figure 4c, the y-axis scale is shifted so that the minimum is at* $d = 0$ *for the three curves. The* $d(\varepsilon)$ *curves without y-axis shift are provided in Figure S8 on the whole strain range.*

3.3 WAXS patterns, evolution of the (001) reflection

3.3.1 Qualitative Description of WAXS Patterns

Examples of X-ray patterns showing the evolution of the (001) reflection as a function of strain are shown in Figure 5 (120°C), Figure S10 (150°C) and Figure S11 (180°C). At the initial state ($\varepsilon = 0$), the intensity is uniform along the diffraction circular ring. At larger strains, two features characterize the change of shape affecting this ring. Firstly, an intensity maximum appears along the ring and the intensity is no longer uniformly distributed, which are typical features of crystal reorientations that occur during the lamellar-fibrillar transition. Secondly, the ring is no longer perfectly circular. This means that the apparent (001) lattice spacing depends on the azimuthal angle φ, which will be interpreted in section 3.5 by analyzing how the α–β transition depends on the crystal orientation.

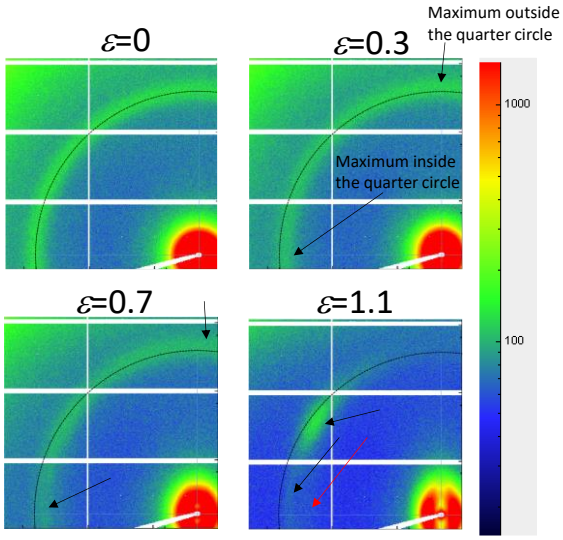

Figure 5 Examples of patterns showing the evolution of the shape of the (001) ring (T=120°C). Red arrow: unexpected intensity reinforcement.

3.3.2 α–β transition

All the reflections present in the patterns that were measured at the initial state ($\varepsilon = 0$) were successfully indexed using the unit cell parameters of the PBT α-form given by Huo et al. [45] which takes in account the temperature dependence of the parameters (see Table 1 for the reflections visible on the pattern of Figure S6a, T = 150°C, distance sample/detector: 726 mm).

	(001)	(01$\bar{1}$)	(010)	($\bar{1}$11)	(1$\bar{1}$0)	(100)	Crystal and smectic structures
Initial state ($\varepsilon = 0$), **measurements** at 150 °C (Å)	9.92	5.66	5.20	4.38	NM	3.85	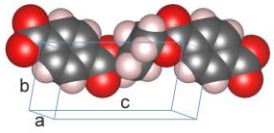 α –form
α –form, **calculated** from Huo et al. for 150 °C (Å)	9.75	5.64	5.19	4.38	4.27	3.85	
Large strain ($\varepsilon = 1.2$), **measurements** at 150 °C (Å)	10.37	5.59	5.18	4.04	NM	3.76	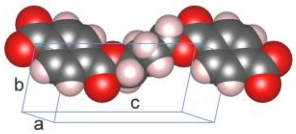 β –form
β –form, **calculated** from Desborough Hall (Å)	10.31	5.59	5.17	4.09	3.91	3.73	
Smectic phase layer period (d_{SP}, Å), **measurements** for $\varepsilon > 0.7$ at the three temperatures.	≈ 12.0 (001′ reflection)						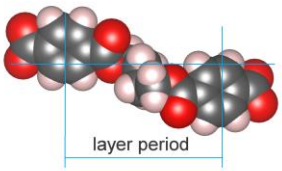 Smectic

Table 1 Calculated and measured lattice spacings. The crystal lattice spacing measurements were obtained from Figures S6a (initial state, $\varepsilon = 0$) and 6b (highly deformed state, $\varepsilon = 1.2$). The (1$\bar{1}$ 0) reflection appears like an inconspicuous shoulder in the ($\bar{1}$ 11) peak and the corresponding lattice spacing is not measurable (NM). The calculated lattice spacings were obtained using the PBT unit cell parameter given by Huo et al. [45] *at 150°C for the α-form (a=4.95 Å, b=6.09 Å, c=11.92 Å, α=100.9°, β=116.2° and γ=110.8°), and by Desborough et Hall.*[24] *for the β-form (a=4.73 Å, b=5.83 Å, c=12.90 Å, α=101.9°, β=119.4° and γ=105.1°). The last line corresponds to the smectic phase evidenced at high strains (see section 3.6).*

In Figure S6b, we show an example of X-ray scattering pattern obtained now at large strain (ε =1.2). The pattern reveals a strongly oriented morphology where the intensities associated with each reflection becomes concentrated at given azimuthal angles. Lattice spacings were calculated by measuring the peak positions in the pattern parts where the signal is concentrated (Table 1). The unit cell parameters of the α–form do not permit to index the experimental measurements at ε =1.2. However, a very good agreement was found using those of the β–form that are given in Desborough et Hall [24] (Table 1) in

the case of a highly oriented PBT. Although the slight dependence of the unit cell parameters on temperature was not studied in the Desborough et Hall article, they were demonstrated to be more efficient at fitting experimental data than others cell parameters previously published [22].

These results demonstrates that the α–β transition effectively takes place during the deformation process. At the end of the test, the strong intensity concentrations in the WAXS patterns correspond to the β form and can be considered as predominant at large strains.

By WAXS analysis of fiber patterns corresponding to the PBT β triclinic morphology, Yokouchi et al. found that the average direction (*c* axis of the triclinic unit cell) of the chains in crystals are along the drawing axis [22]. In Figure S6b and S12 corresponding to large strains, it can be checked that the intensities corresponding to the (hk0) reflections—those of the planes that contain the chain direction—are concentrated along the vertical axis, which is perpendicular to the drawing direction (φ=90°). This confirms that the chain average directions in crystals are well along the drawing axis at large strains. To get a better understanding of the mechanism of polymer chain orientation and of the α–β transition (upon deformation at elevated temperature), the following sections (3.4 and 3.5) focuses on analyzing the evolution of the (001) reflection during tests.

3.4 Analysis of polymer orientation through the (001) and the SAXS patterns

In Figure 5, Figures S10 and S11, the reorientation of the (001) reflection is clearly visible at large strains ($\varepsilon = 1.1$). The intensity is then concentrated around a maximum situated at ($\varphi = 38°$), which is in good agreement with the value ($\varphi = 37°$) that can be calculated using the unit cell parameters of the β triclinic form,[23] and assuming that the *c* axis is along the drawing direction.

In order to evaluate the crystal reorientation rate, we have calculated the Herman factor: $H^{001} = \left(3\left\langle \cos^2 \varphi \right\rangle - 1\right)/2$. $H^{001} = 0$ when the lattice orientation is uniformly distributed. When the chains in crystals are oriented along the drawing direction, the final azimuthal angle value is approximately 38°, and the expected value for the Hermann factor should be $H^{001} \approx 0.42$.

The evolution of H^{001} is shown in Figure 6 for the three test temperatures. The three stages of the deformation process — separated by the same temperature-independent thresholds — can again be identified on the $H^{001}(\varepsilon)$. During strain range *I* ($\varepsilon < 0.3$), when the lamellar morphology is approximately preserved, H^{001} slightly decreases. This may be caused by the formation of a "kink morphology", which corresponds to local disorientation of the lamellae with normal initially oriented along the drawing axis. The occurring of kink (or chevron) morphology in the spherulite equatorial parts has often been reported [46–48]. This can be interpreted as a form of buckling due to the existence of a compressive stress along the lamellae of these regions. Logically, H^{001} strongly increases during the transition between the lamellar and fibrillar morphologies (strain range *II*, $0.3 < \varepsilon < 1$). During strain range *III*, crystal reorientation continues but the $H^{001}(\varepsilon)$ slope is slightly reduced. If the tensile test were to be continued, H^{001} would likely increase to the 0.42 value that corresponds to fully oriented crystals. The polymer orientation was also analyzed from the SAXS patterns using an orientation parameter A that was calculated as follows:

$$A = \frac{I_{SAXS}^{H} - I_{SAXS}^{V}}{I_{SAXS}^{H} + I_{SAXS}^{V}}$$

Equation 2

I_{SAXS}^{H} and I_{SAXS}^{V} are the average intensities in angular sectors corresponding respectively to $\varphi = [0° \quad 10°]$ and $\varphi = [80° \quad 90°]$, and limited to a q range that includes almost all the intensity specifically scattered by lamellae ($q = [0.015 \quad 0.2]\,Å^{-1}$). $A = 0$ in the case of the isotropically disoriented lamellar morphology. When the fibrillar morphology is being formed, the intensity of the lamellar peak concentrates along the horizontal axis, which leads to an increase of A.

In order to compare the SAXS and WAXS results as in Tashiro et al. [49], we plotted the $A(\varepsilon)$ in the same figure as those corresponding to the Herman factor H^{001} (Figure 6). $H^{001}(\varepsilon)$ and $A(\varepsilon)$ clearly

show the same trends The three regimes (*I*, *II* and *III*) also clearly appear on the $A(\varepsilon)$ curves and are separated by the same previously identified strain thresholds ($\varepsilon \approx 0.3$ and $\varepsilon \approx 1.0$).

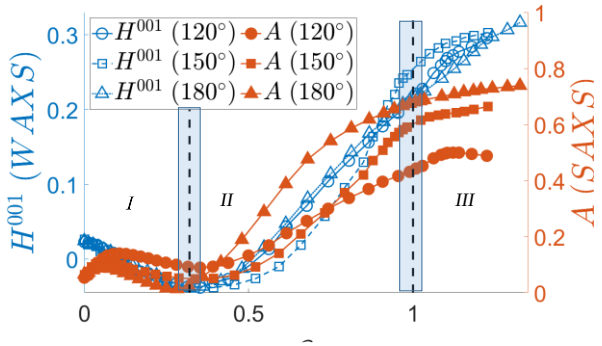

Figure 6 Orientation parameters extracted from the (001) reflection (H^{001}) and SAXS patterns (A).

3.5 Analysis of the α–β transition as a function of the crystal orientation

To visualize clearly the lattice spacing changes along the (001) ring, we have plotted an identical quarter circle in dotted lines on all the patterns corresponding to the same temperature (Figure 5, S10 and S11). At $\varepsilon = 0$, this quarter circle corresponds to the position of the intensity maxima along the ring. At $\varepsilon = 0.3$, the intensity maxima are respectively situated inside and outside the reference quarter circle in the horizontal ($\varphi \approx 0$) and vertical ($\varphi \approx 90°$) pattern parts. This means that the (001) plane spacing is increased when the normal to these planes is close to the tensile axis while it is decreased when it is perpendicular to this direction. At $\varepsilon = 0.7$, the intensity maximum of the (001) reflection along the horizontal axis has moved even closer to the beam stop (ring center). In Figure 7, we have plotted the lattice spacing against the azimuthal angle $d_{001}(\varphi)$ for different strains at 120°C, as well as the expected d_{001} values for the α and β forms. The $d_{001}(\varphi)$ curves were obtained by finding the q position of the peak associated with the (001) reflection at a given value of the azimuthal angle φ. Because the corresponding q values are close, and because as it will be shown thereafter these two phases are intrinsically slightly deformable along the normal to the (001) planes, it was not possible to separate the two peaks that are associated with the α and β forms. Therefore, the continuous variations of d_{001}

between the expected values for these two phases that are observed roughly for φ <50°—when the macro-elongation along the normal to the lattices is positive (see paragraph SI5 in the supplementary information)—show that these two crystalline forms can coexist for crystals with the same orientation. The β form becomes predominant when $\varphi \to 0$, that is to say when the stress and macro-elongation along the normal to the (001) lattices is maximum. For $\varphi = 0°$, d_{001} is even larger than the value (10.31 *Å*) corresponding to the β phase. The unit cell parameters that we used for this triclinic phase were determined on a strongly oriented structure,[23] which corresponds to φ=38° for the (001) reflection, an orientation for which the stress ($\sigma \cos^2 \varphi$) along the normal to the considered lattices is significantly reduced compared to $\varphi = 0$. After the formation of the β structure, d_{001} remains therefore slightly extensible when the strain (and stress) is applied along the normal to the (001) lattices with a maximum possible value around 10.55 *Å*. For lattice orientations subjected to negative macro-elongation along their normal vector (roughly φ>65°, see paragraph SI5 in the supplementary information), d_{001} becomes a bit lower than the value corresponding to the α triclinic structure (9.92 *Å*) with a minimum value of about 9.85 *Å*. Here again, the α crystals are slightly deformable even in the absence of any possible phase change.

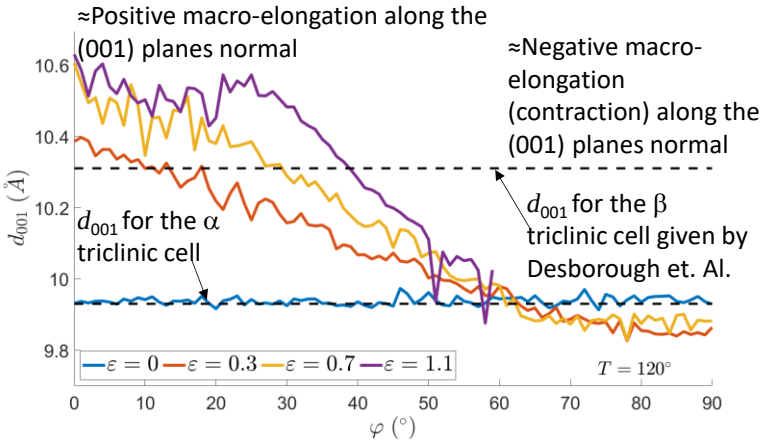

Figure 7 d_{001} *versus the azimuthal angle along the (001) reflection ring at different strains.*

In the following, we use the formalism presented in paragraph SI5 to analyze further and quantitatively the relationship between the macro-scale deformation and the evolution of d_{001} in link with the α→β transition. During strain range *I*, i.e. before the yield strain, the integrity of the lamellar morphology is considered as preserved and no breakage in crystals occurs. We therefore assume that the changes of the (001) lattice normal directions with respect to the drawing axis are the same as that of the macroscopic directions that coincide at the initial state (ψ_0). This means that $\psi(\psi_0,\varepsilon)=\psi_L(\psi_0,\varepsilon)$ with the notations defined in sections 2.2.2 and paragraph SI5 of the supplementary information. It should also be noted that the orientation of the (001) lattices only slightly change during the α→β transition, from 35° to 36.5° with respect to the chain direction (*c*).

As detailed in SI5, we can calculate $\psi(\psi_0,\varepsilon)$ (see Figure S13), and using $\varphi\approx\psi$ (section 2.2.2) extract the local elongation in crystals from patterns: $e_{crys}(\psi_0,\varepsilon)=\left[d_{001}^{\psi}(\varepsilon)-d_{001}^{\psi_0}(0)\right]/d_{001}^{\psi_0}(0)$. $d_{001}^{\psi_0}(0)$ is the (001) lattice spacing at the initial state ($\varepsilon=0$) in a crystal oriented so that the normal to the (001) plane makes an initial angle ψ_0 with respect to the drawing axis. $d_{001}^{\psi}(\varepsilon)$ is the (001) lattice spacing during deformation for the same crystal when the angle between the normal and the drawing axis has changed from ψ_0 to ψ. The objective is to analyze the link of $e_{crys}(\psi_0,\varepsilon)$ with the macro-elongation $e_{macro}(\psi_0,\varepsilon)=\left[\ell^{\psi}(\varepsilon)-\ell^{\psi_0}(0)\right]/\ell^{\psi_0}(0)$ (see Figure S14). As detailed in SI5, $\ell^{\psi_0}(0)$ and $\ell^{\psi}(\varepsilon)$ are the initial and current lengths of an element defined on the macro-scale that makes an initial angle ψ_0, and a current angle ψ, with respect to the drawing axis (same angle variation ($\psi_0\rightarrow\psi$) as the normal to the considered (001) lattices). The evolution of e_{crys} versus ε is plotted for various ψ_0 initial angles in Figure 8 (120°C), S14 (150°C) and S15 (180°C). When the macro-elongation e_{macro} is positive during strain range *I* ($\varepsilon<0.3$), plain circles symbol are used (ψ_0=0°, 20°, 40° and 50°, Figure S14) whilst it is plain triangles otherwise ($e_{macro}<0$; $\psi_0=80°$ and 90°, see Figure S14). For $\psi_0=65°$, $e_{macro}\approx 0$ during stage I (Figure S14) and we used plain squares for the plot.

The comments about the curves representing e_{crys} against ε (Figures 8, S15 and S16) are consistent with those corresponding to Figure 7. When e_{macro} is positive, e_{crys} is also positive (plain circle curves), and the larger e_{macro} ($\Leftrightarrow$ the smaller ψ_0) the larger e_{crys}. On the other hand, if e_{macro} is negative, e_{crys} is also negative (plain triangle curves). When e_{macro} is very close to 0, e_{crys} is also very close to 0 (plain square curve). For further analysis, we plotted $|e_{crys}|$ against $|e_{macro}|$ (Figure 9: 120°C, Figure S17: 150°C and Figure S18: 180°C). Strikingly, if $\psi_0 \leq 50°$, all the curves fall on the same master curve. This means that if $e_{macro} > 0$, the average elongation (e_{crys}) in crystals along the (001) lattice normal only depends on the macro elongation (e_{macro}) along this direction. At 120°C, e_{crys} approximately reaches the value corresponding to the β structure when $e_{macro} \approx 0.3$., which corresponds to $d_{001} = 10.31 Å$ or $e_{crys} \approx 0.04$. Overall, the relative proportion of each of the two phases appears to be controlled by the macro-elongation applied along the normal to the (001) lattices. For $e_{macro} = 0.3$, e_{macro} is respectively 7.2, 8.0 and 10.3 times larger than e_{crys} at 120°C (Figure 9), 150°C (Figure S17) and 180°C (Figure S18). This confirms that deformation mainly takes place in the interlamellar amorphous regions. At 150°C and 180°C, e_{crys} does not reach the value corresponding to the β form at $e_{macro} = 0.3$. However, the significant increase of e_{crys}, average value between the α and β forms (because the corresponding peaks are not separated), shows that the phase transition has well begun. Except at very small strains ($|e_{macro}| < 0.02$), if $e_{macro} < 0$ the dependence of e_{crys} on e_{macro} differs from that observed when $e_{macro} > 0$, the e_{crys} / e_{macro} ratio is smaller. The e_{crys} decrease is then only due to the compressibility of the α crystals, no phase transition is involved.

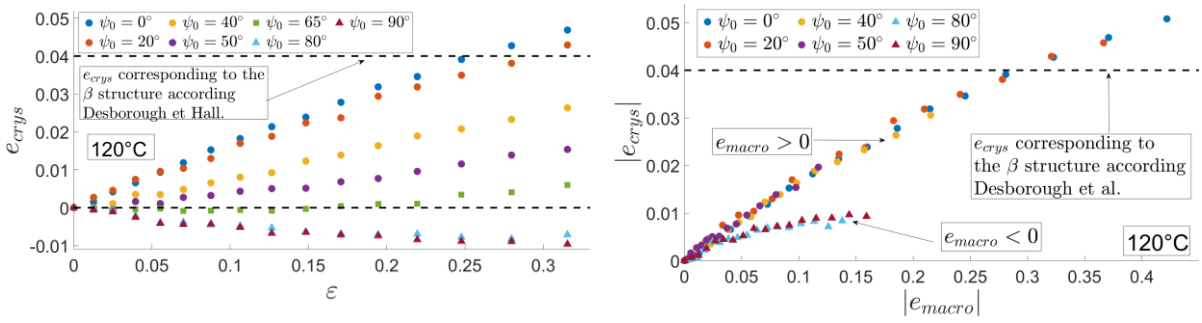

Figure 8 Evolution of the local elongations versus ε. ψ_0 is the initial angle between the normal to the (001) lattices and the drawing axis.

Figure 9 Local elongations versus macro-elongations. Results provided in absolute values. (T=120°C).

3.6 Evidences of the development of a mesomorphic phase at large strains

At larger strains and for small φ angles, a new weak and unexpected peak was detected (indicated by a red arrow in Figure 5 or Figure S6b). Its presence was enhanced in the right part of Figure 10e ($\varepsilon = 1.28$ at 120°C) with a modified color scale. Similarly, this new peak can also be observed at the ends of the tests performed at 150°C and 180°C (see Figure S19). Its appearance and growth become very clear by plotting the $I(q)$ intensity profiles measured at different strains for $\varphi = 0°$ (Figure 10). On these profiles, a deconvolution procedure was implemented to separate the new peak from that associated with the (001) reflection. The new peak (denoted SP) can clearly be extracted from the noisy intensity signal for strains larger than $\varepsilon = 0.3$ or $\varepsilon = 0.4$, when the polymer orientation begins (Figure 6). Next, it grows as the strain increases and its maximum becomes higher than that of the (001) reflection at the end of the test ($\varepsilon = 1.28$). We plotted in the same figure (Figure S20) the correlation distance evolutions for the two peaks: d_{SP} (New Peak) and d_{001}. d_{SP} starts to be measurable approximately at $\varepsilon \approx 0.4$, and then remains approximately constant, even if a slight increase trend can be detected at the test ends, precisely at the strain threshold $\varepsilon = 1$ when the fibrillar morphology is established and the polymer chains taut. We found the following values for d_{SP} at 120°C, 150°C and 180°C: $11.9\ Å$, $11.9\ Å$ and $12.0\ Å$ respectively. At each temperature these values were averaged in the $\varepsilon = [0.6\ 0.8]$ interval where the new peak is accurately extracted from the noise.

The smectic peaks that have already been observed in amorphous polyester subjected to stretching below T_g are situated along the drawing axis [28–32]. In the case of PBT, this peak corresponds to a $11.7\ Å$ correlation distance [28,29]. The peak appearing at large strains and $\varphi \approx 0$ (drawing axis) in Figure 10 can therefore be identified as the smectic phase already reported for PBT. The slight discrepancy in

correlation distance — $\approx 11.9\text{Å} - 12\ \text{Å}$ in the 120°-180° range instead of $11.7\ \text{Å}$ at room temperature — can be attributed to thermal expansion. A schematic representation of the smectic structure is shown in Table 1. The layer period (d_{SP}) is equal to the distance between dense planes where aromatic cycles are concentrated. One can consider that this distance corresponds to the average spacing between two aromatic cycles along a PBT chain with liquid like disorder. This helps to understand why d_{SP} ($\approx 11.9\text{Å} - 12\ \text{Å}$) is very close to the c parameter (11.92Å) of the α triclinic cell, which is also a distance between aromatic cycles (see Table 1 where the α cell is also represented). Of note, the smectic phase is here observed well above T_g during stretching of an initially crystallized polymer, and not starting from an amorphous polymer. This transition is likely induced by ordering of the amorphous fraction upon application of stress on the physical network formed by crystal nodes.

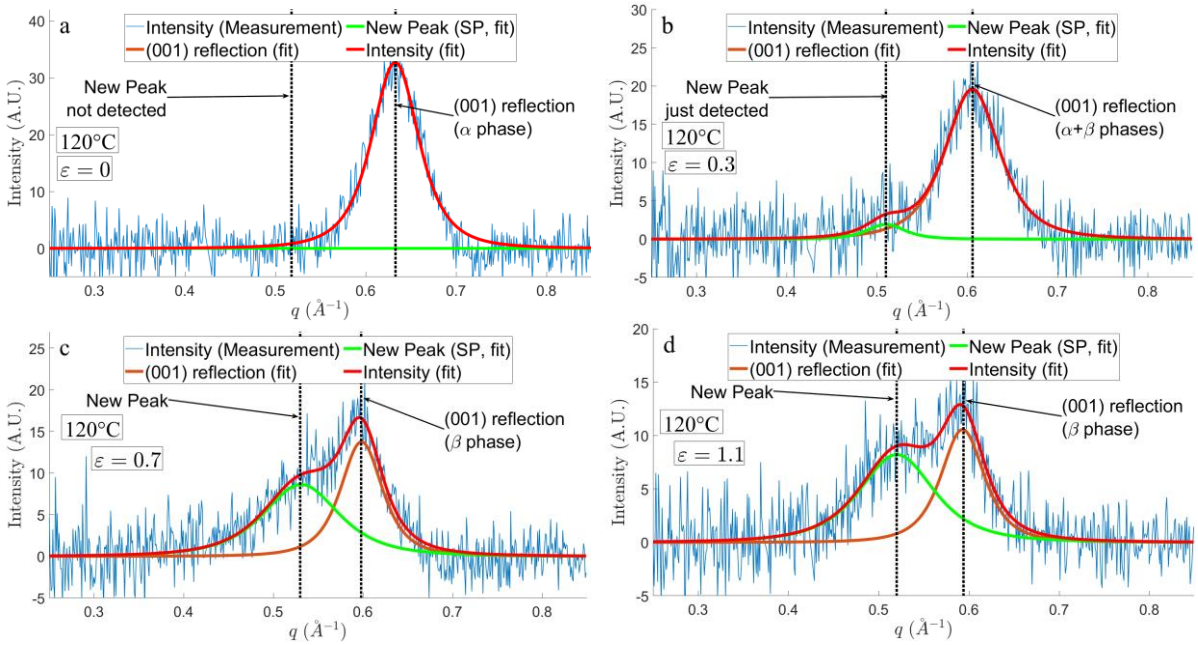

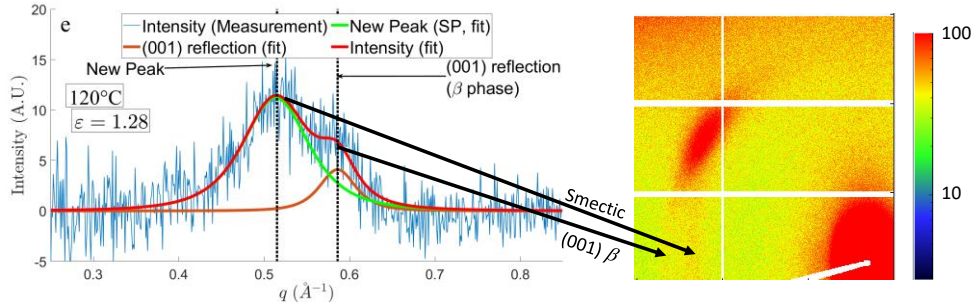

Figure 10 Appearance of a smectic phase $I(q)$ *profiles plotted at* $\varphi = 0°$ *in the* $q = [0.25\ 0.85]\,Å^{-1}$ *interval at* $\varepsilon = 0$ *(a),* $\varepsilon = 0.3$ *(b),* $\varepsilon = 0.7$ *(c),* $\varepsilon = 1.1$ *(d) and* $\varepsilon = 1.28$ *(e) for a test carried out at 120°C. The deconvolution procedure to separate the new peak (SP) from the (001) reflection is illustrated in the figure. In the right part of Figure 13e, we also show the image of the corresponding pattern as well as the position of the new peak.*

Conclusion

Synchrotron X-ray scattering experiments were performed at 120°C, 150°C and 180°C to study the deformation mechanisms in PBT. The deformation process was found to occur in three stages, separated by temperature-independent macroscopic strain thresholds measured in the specimen center by image correlation, precisely in the cross section where the X-ray scattering measurements are performed. Another original result concerns the α→β transition that was studied from the evolution of the (001) lattice spacing as a function of the crystal orientation. It was found that the α→β transition is fully governed by the macroscopic elongation along the normal vector to these lattices. Finally, the development of a smectic phase was observed at large strains above T_g, in conditions never reported before. This study allows us to set clear true strain boundaries between the different deformation regimes of PBT and understand the underlying mechanisms when subjected to high-temperature tensile deformation. This helps us to better predict the behavior of this material when it is used in everyday life (e.g., in electrical insulation or kitchen tools). It is also a necessary preliminary step before implementing strategies such as vitrimerization aimed at improving its mechanical and rheological properties.

Acknowledgments

The authors would like to thank the ICEEL Carnot Institute, the EMPP research department of Lorraine University, the Grand Est Region and ADEME (French agency for ecological transition) for their financial support.

We are also very grateful to Camille Noûs and Diego Ciardi for helping prepare and carry out these experiments. We are also very grateful to the staff of the SWING beamline at SOLEIL for their assistance during the experiments.

Preliminary experiments have been performed at the DND-CAT 5ID-D beamline at Argonne National Laboratory under Contract DE-AC02-06CH11357. We thank Steven J. Weigand for performing these measurements.

References

[1] A. Demongeot, R. Groote, H. Goossens, T. Hoeks, F. Tournilhac, L. Leibler, Cross-Linking of Poly(butylene terephthalate) by Reactive Extrusion Using Zn(II) Epoxy-Vitrimer Chemistry, Macromolecules. 50 (2017) 6117–6127. https://doi.org/10.1021/acs.macromol.7b01141.

[2] Y. Zhou, J.G.P. Goossens, R.P. Sijbesma, J.P.A. Heuts, Poly(butylene terephthalate)/Glycerol-based Vitrimers via Solid-State Polymerization, Macromolecules. 50 (2017) 6742–6751. https://doi.org/10.1021/acs.macromol.7b01142.

[3] Y. Zhou, J.G.P. Goossens, S. Van Den Bergen, R.P. Sijbesma, J.P.A. Heuts, In Situ Network Formation in PBT Vitrimers via Processing-Induced Deprotection Chemistry, Macromol. Rapid Commun. 39 (2018) 1800356. https://doi.org/10.1002/marc.201800356.

[4] Y. Zhou, R. Groote, J.G.P. Goossens, R.P. Sijbesma, J.P.A. Heuts, Tuning PBT vitrimer properties by controlling the dynamics of the adaptable network, Polym. Chem. 10 (2019) 136–144. https://doi.org/10.1039/C8PY01156G.

[5] L. Farge, S. Hoppe, V. Daujat, F. Tournilhac, S. André, Solid Rheological Properties of PBT-Based Vitrimers, Macromolecules. 54 (2021) 1838–1849. https://doi.org/10.1021/acs.macromol.0c02105.

[6] L. Farge, R. Spiegel, S. André, C. Noûs, R. Lainé, S. Hoppe, Development of plasticity in vitrimers synthesized from a semi-crystalline polymer using injection molding, J. Polym. Sci. 60 (2022) 1962–1975. https://doi.org/10.1002/pol.20220062.

[7] M.F. Butler, A.M. Donald, W. Bras, G.R. Mant, G.E. Derbyshire, A.J. Ryan, A Real-Time Simultaneous Small- and Wide-Angle X-ray Scattering Study of In-Situ Deformation of Isotropic Polyethylene, Macromolecules. 28 (1995) 6383–6393. https://doi.org/10.1021/ma00123a001.

[8] M.F. Butler, A.M. Donald, A.J. Ryan, Time resolved simultaneous small- and wide-angle X-ray scattering during polyethylene deformation: 1. Cold drawing of ethylene- -olefin copolymers, (n.d.).

[9] D.J. Hughes, A. Mahendrasingam, W.B. Oatway, E.L. Heeley, C. Martin, W. Fuller, A simultaneous SAXS/WAXS and stress-strain study of polyethylene deformation at high strain rates, Polymer. 38 (1997) 6427–6430. https://doi.org/10.1016/S0032-3861(97)00351-0.

[10] M.F. Butler, A.M. Donald, A.J. Ryan, Time resolved simultaneous small- and wide-angle X-ray scattering during polyethylene deformation—II. Cold drawing of linear polyethylene, Polymer. 39 (1998) 39–52. https://doi.org/10.1016/S0032-3861(97)00226-7.

[11] B. Xiong, O. Lame, J.M. Chenal, C. Rochas, R. Seguela, G. Vigier, In-situ SAXS study and modeling of the cavitation/crystal-shear competition in semi-crystalline polymers: Influence of temperature and microstructure in polyethylene, Polymer. 54 (2013) 5408–5418. https://doi.org/10.1016/j.polymer.2013.07.055.

[12] B. Xiong, O. Lame, J.-M. Chenal, C. Rochas, R. Seguela, G. Vigier, Temperature-Microstructure Mapping of the Initiation of the Plastic Deformation Processes in Polyethylene via In Situ WAXS and SAXS, Macromolecules. 48 (2015) 5267–5275. https://doi.org/10.1021/acs.macromol.5b01258.

[13] S. Yakovlev, D. Fiscus, P. Brant, J. Butler, D.G. Bucknall, K.H. Downing, Mechanism of stress induced crystallization of polyethylene, Polymer. 175 (2019) 25–31. https://doi.org/10.1016/j.polymer.2019.04.054.

[14] Y. Lin, X. Li, X. Chen, M. An, Q. Zhang, D. Wang, W. Chen, P. Yin, L. Meng, L. Li, Deformation mechanism of hard elastic polyethylene film during uniaxial stretching: Effect of stretching speed, Polymer. 178 (2019) 121579. https://doi.org/10.1016/j.polymer.2019.121579.

[15] Y. Lin, X. Li, X. Chen, M. An, Q. Zhang, D. Wang, W. Chen, L. Sun, P. Yin, L. Meng, L. Li, Structural evolution of hard-elastic polyethylene cast film in temperature-strain space: An in-situ SAXS and WAXS study, Polymer. 184 (2019) 121930. https://doi.org/10.1016/j.polymer.2019.121930.

[16] R.J. Davies, N.E. Zafeiropoulos, K. Schneider, S.V. Roth, M. Burghammer, C. Riekel, J.C. Kotek, M. Stamm, The use of synchrotron X-ray scattering coupled with in situ mechanical testing for studying deformation and structural change in isotactic polypropylene, Colloid Polym. Sci. 282 (2004) 854–866. https://doi.org/10.1007/s00396-004-1118-z.

[17] J. Qiu, Z. Wang, L. Yang, J. Zhao, Y. Niu, B.S. Hsiao, Deformation-induced highly oriented and stable mesomorphic phase in quenched isotactic polypropylene, Polymer. 48 (2007) 6934–6947. https://doi.org/10.1016/j.polymer.2007.08.066.
[18] A. Pawlak, A. Galeski, Cavitation during Tensile Deformation of Polypropylene, Macromolecules. 41 (2008) 2839–2851. https://doi.org/10.1021/ma0715122.
[19] Z. Cai, Y. Zhang, J. Li, F. Xue, Y. Shang, X. He, J. Feng, Z. Wu, S. Jiang, Real time synchrotron SAXS and WAXS investigations on temperature related deformation and transitions of β-iPP with uniaxial stretching, Polymer. 53 (2012) 1593–1601. https://doi.org/10.1016/j.polymer.2012.02.012.
[20] X. Chen, F. Lv, F. Su, Y. Ji, L. Meng, C. Wan, Y. Lin, X. Li, L. Li, Deformation mechanism of iPP under uniaxial stretching over a wide temperature range: An in-situ synchrotron radiation SAXS/WAXS study, Polymer. 118 (2017) 12–21. https://doi.org/10.1016/j.polymer.2017.04.054.
[21] W. Zhang, J. Li, H. Li, S. Jiang, L. An, Temperature dependence of deformation behavior of poly(butylene terephthalate), Polymer. 143 (2018) 309–315. https://doi.org/10.1016/j.polymer.2018.04.030.
[22] M. Yokouchi, Y. Sakakibara, Y. Chatani, H. Tadokoro, T. Tanaka, K. Yoda, Structures of Two Crystalline Forms of Poly(butylene terephthalate) and Reversible Transition between Them by Mechanical Deformation, Macromolecules. 9 (1976) 266–273. https://doi.org/10.1021/ma60050a018.
[23] R. Jakeways, I.M. Ward, M.A. Wilding, I.H. Hall, I.J. Desborough, M.G. Pass, Crystal deformation in aromatic polyesters, J. Polym. Sci. Polym. Phys. Ed. 13 (1975) 799–813. https://doi.org/10.1002/pol.1975.180130412.
[24] I.J. Desborough, I.H. Hall, A comparison of published crystalline structures of poly(tetramethylene terephthalate), Polymer. 18 (1977) 825–830. https://doi.org/10.1016/0032-3861(77)90189-6.
[25] M.G. Brereton, G.R. Davies, R. Jakeways, T. Smith, I.M. Ward, Hysteresis of the stress-induced crystalline phase transition in poly(butylene terephthalate), Polymer. 19 (1978) 17–26. https://doi.org/10.1016/0032-3861(78)90166-0.
[26] K. Tashiro, Y. Nakai, M. Kobayashi, H. Tadokoro, Solid-State Transition of Poly(butylene terephthalate) Induced by Mechanical Deformation, Macromolecules. 13 (1980) 137–145. https://doi.org/10.1021/ma60073a026.
[27] P.L. Carr, R. Jakeways, J.L. Klein, I.M. Ward, Tensile drawing, morphology, and mechanical properties of poly(butylene terephthalate), J. Polym. Sci. Part B Polym. Phys. 35 (1997) 2465–2481. https://doi.org/10.1002/(SICI)1099-0488(19971115)35:15<2465::AID-POLB9>3.0.CO;2-S.
[28] K. Song, Formation of polymorphic structure and its influences on properties in uniaxially stretched polybutylene terephthalate films, J. Appl. Polym. Sci. 78 (2000) 412–423. https://doi.org/10.1002/1097-4628(20001010)78:2<412::AID-APP210>3.0.CO;2-E.
[29] T. Konishi, Y. Miyamoto, Smectic structure and glass transition in poly(butylene terephthalate), Polym. J. 42 (2010) 349–353. https://doi.org/10.1038/pj.2010.5.
[30] D. Kawakami, B.S. Hsiao, C. Burger, S. Ran, C. Avila-Orta, I. Sics, T. Kikutani, K.I. Jacob, B. Chu, Deformation-Induced Phase Transition and Superstructure Formation in Poly(ethylene terephthalate), Macromolecules. 38 (2005) 91–103. https://doi.org/10.1021/ma049333x.
[31] T. Sago, H. Itagaki, T. Asano, Onset of Forming Ordering in Uniaxially Stretched Poly(ethylene terephthalate) Films Due to π–π Interaction Clarified by the Fluorescence Technique, Macromolecules. 47 (2014) 217–226. https://doi.org/10.1021/ma401806u.
[32] R. Jakeways, J.L. Klein, I.M. Ward, The existence of a mesophase in poly(ethylene naphthalate), Polymer. 37 (1996) 3761–3762. https://doi.org/10.1016/0032-3861(96)00113-9.
[33] G.R. Strobl, M.J. Schneider, I.G. Voigt-Martin, Model of partial crystallization and melting derived from small-angle X-ray scattering and electron microscopic studies on low-density polyethylene, J. Polym. Sci. Polym. Phys. Ed. 18 (1980) 1361–1381. https://doi.org/10.1002/pol.1980.180180615.
[34] Y. Huang, X. Xia, Z. Liu, W. Yang, C. Zhu, D. Xie, R. Chen, M. Yang, The formation of interfacial morphologies of iPP derived from transverse flow during multi-penetration in secondary melt flow, Mater. Today Commun. 12 (2017) 43–54. https://doi.org/10.1016/j.mtcomm.2017.06.005.

[35] Haward, R.N., Thackray, G., The use of a mathematical model to describe isothermal stress-strain curves in glassy thermoplastics, Proc. R. Soc. Lond. Ser. Math. Phys. Sci. 302 (1968) 453–472. https://doi.org/10.1098/rspa.1968.0029.
[36] R.N. Haward, Strain hardening of thermoplastics, Macromolecules. 26 (1993) 5860–5869. https://doi.org/10.1021/ma00074a006.
[37] J. Ye, S. André, L. Farge, Kinematic study of necking in a semi-crystalline polymer through 3D Digital Image Correlation, Int. J. Solids Struct. 59 (2015) 58–72. https://doi.org/10.1016/j.ijsolstr.2015.01.009.
[38] L. Farge, S. André, J. Boisse, Use of Digital Image Correlation to study the effect of temperature on the development of plastic instabilities in a semi-crystalline polymer, Polymer. 153 (2018) 295–304. https://doi.org/10.1016/j.polymer.2018.07.076.
[39] N. Stribeck, D. Sapoundjieva, Z. Denchev, A.A. Apostolov, H.G. Zachmann, M. Stamm, S. Fakirov, Deformation Behavior of Poly(ether ester) Copolymer As Revealed by Small- and Wide-Angle Scattering of X-ray Radiation from Synchrotron, Macromolecules. 30 (1997) 1329–1339. https://doi.org/10.1021/ma9612079.
[40] Z. Jiang, Y. Tang, J. Rieger, H.-F. Enderle, D. Lilge, S.V. Roth, R. Gehrke, Z. Wu, Z. Li, Y. Men, Structural evolution of tensile deformed high-density polyethylene at elevated temperatures: Scanning synchrotron small- and wide-angle X-ray scattering studies, Polymer. 50 (2009) 4101–4111. https://doi.org/10.1016/j.polymer.2009.06.063.
[41] T. Liao, Z. Jiang, R. Li, Y. Gao, Y. Men, Stretching temperature dependence of the critical strain in the tensile deformation of polyethylene copolymer, Eur. Polym. J. 97 (2017) 188–197. https://doi.org/10.1016/j.eurpolymj.2017.10.015.
[42] B. Chang, K. Schneider, F. Xiang, R. Vogel, S. Roth, G. Heinrich, Critical Strains for Lamellae Deformation and Cavitation during Uniaxial Stretching of Annealed Isotactic Polypropylene, Macromolecules. 51 (2018) 6276–6290. https://doi.org/10.1021/acs.macromol.8b00642.
[43] J.C. Habumugisha, S. Feng, O. Iqbal, Y. Lin, M. An, L. Meng, D. Wang, W. Chen, L. Li, Stretch-induced structural evolution of pre-oriented isotactic polypropylene films: An in-situ synchrotron radiation SAXS/WAXS study, Polymer. 214 (2021) 123234. https://doi.org/10.1016/j.polymer.2020.123234.
[44] Y. Mao, D.G. Bucknall, R.M. Kriegel, Simultaneous WAXS/SAXS study on semi-crystalline Poly(ethylene furanoate) under uniaxial stretching, Polymer. 143 (2018) 228–236. https://doi.org/10.1016/j.polymer.2018.04.018.
[45] P.P. Huo, P. Cebe, M. Capel, Real-time X-ray scattering study of thermal expansion of poly(butylene terephthalate), J. Polym. Sci. Part B Polym. Phys. 30 (1992) 1459–1468. https://doi.org/10.1002/polb.1992.090301305.
[46] A. Galeski, Z. Bartczak, A.S. Argon, R.E. Cohen, Morphological alterations during texture-producing plastic plane strain compression of high-density polyethylene, Macromolecules. 25 (1992) 5705–5718. https://doi.org/10.1021/ma00047a023.
[47] M. Krumova, S. Henning, G.H. Michler, Chevron morphology in deformed semicrystalline polymers, Philos. Mag. 86 (2006) 1689–1712. https://doi.org/10.1080/14786430500501671.
[48] A. Pawlak, A. Galeski, A. Rozanski, Cavitation during deformation of semicrystalline polymers, Prog. Polym. Sci. 39 (2014) 921–958. https://doi.org/10.1016/j.progpolymsci.2013.10.007.
[49] K. Tashiro, H. Yamamoto, T. Yoshioka, T.H. Ninh, M. Tasaki, S. Shimada, T. Nakatani, H. Iwamoto, N. Ohta, H. Masunaga, Hierarchical Structural Change in the Stress-Induced Phase Transition of Poly(tetramethylene terephthalate) As Studied by the Simultaneous Measurement of FTIR Spectra and 2D Synchrotron Undulator WAXD/SAXS Data, Macromolecules. 47 (2014) 2052–2061. https://doi.org/10.1021/ma402041r.